

Journal Pre-proof

Occurrence state and oil content evaluation of Permian Fengcheng Formation in the Hashan area as constrained by NMR and multistage Rock-Eval

Yue Wang, Xiangchun Chang, Zhongquan Liu, Pengfei Zhang, Weizheng Gao, Zhiping Zeng, Guisheng Li



PII: S1995-8226(22)00305-3

DOI: <https://doi.org/10.1016/j.petsci.2022.11.019>

Reference: PETSCI 411

To appear in: *Petroleum Science*

Received Date: 2 June 2022

Revised Date: 29 September 2022

Accepted Date: 22 November 2022

Please cite this article as: Wang, Y., Chang, X., Liu, Z., Zhang, P., Gao, W., Zeng, Z., Li, G., Occurrence state and oil content evaluation of Permian Fengcheng Formation in the Hashan area as constrained by NMR and multistage Rock-Eval, *Petroleum Science* (2022), doi: <https://doi.org/10.1016/j.petsci.2022.11.019>.

This is a PDF file of an article that has undergone enhancements after acceptance, such as the addition of a cover page and metadata, and formatting for readability, but it is not yet the definitive version of record. This version will undergo additional copyediting, typesetting and review before it is published in its final form, but we are providing this version to give early visibility of the article. Please note that, during the production process, errors may be discovered which could affect the content, and all legal disclaimers that apply to the journal pertain.

© 2022 The Authors. Publishing services by Elsevier B.V. on behalf of KeAi Communications Co. Ltd.

Occurrence state and oil content evaluation of Permian Fengcheng Formation in the Hashan area as constrained by NMR and multistage Rock-Eval

Yue Wang¹, Xiangchun Chang^{1,2,*}, Zhongquan Liu³, Pengfei Zhang¹, Weizheng Gao¹, Zhiping Zeng³, Guisheng Li⁴

¹College of Earth Science and Engineering, Shandong University of Science and Technology, Qingdao 266590, China

²Laboratory for Marine Mineral Resources, Pilot National Laboratory for Marine Science and Technology, Qingdao, 266071, China

³Research Institute of Petroleum Exploration and Development, Shengli Oil Company, Sinopec, Dongying, 257001, China

⁴No.5 Oil Production Plant of Dagang Oilfield Company, CNPC, Tianjin, 300280, China

* Corresponding author. Tel.: +86 532 80691766; fax: +86 532 86057219. E-mail address: xcchang@sdust.edu.cn (X. Chang).

Occurrence state and oil content evaluation of the Permian Fengcheng Formation in the Hashan area as constrained by nuclear magnetic resonance and multistage Rock-Eval pyrolysis

Yue Wang¹, Xiangchun Chang^{1,2*}, Zhongquan Liu³, Pengfei Zhang¹, Weizheng Gao¹, Zhiping Zeng³, Guisheng Li⁴, Gang Li⁴

¹College of Earth Science and Engineering, Shandong University of Science and Technology, Qingdao 266590, China

²Laboratory for Marine Mineral Resources, Pilot National Laboratory for Marine Science and Technology, Qingdao, 266071, China

³Research Institute of Petroleum Exploration and Development, Shengli Oil Company, Sinopec, Dongying, 257001, China

⁴No.5 Oil Production Plant of Dagang Oilfield Company, CNPC, Tianjin, 300280, China

*Corresponding author. Tel.: +86 532 80691766; fax: +86 532 86057219. E-mail address: xcchang@sdust.edu.cn (X. Chang).

Abstract

The Hashan area, neighboring the Mahu Sag that is rich in the shale oil resources, showed commercial oil flow in the corresponding lacustrine shales of the Lower Permian Fengcheng Formation (P_{1f}) with reserve scale approximately 789 million tons, presenting great potential for oil exploration. Despite their geographical proximity, the hydrocarbon occurrence and oil-bearing capacity of shale in the Hashan area and Mahu Sag greatly differ owing to the complex tectonic evolution. Therefore, understanding the occurrence state and oil content of the P_{1f} in the Hashan area is crucial for ongoing shale oil exploration activities and the development of the northwestern margin of the

Junggar Basin. In this study, an integrated investigation, including petrological observations, scanning electron microscopy (SEM) observation, analysis of nuclear magnetic resonance (NMR) T_1 – T_2 spectra, and conventional and multistage Rock-Eval pyrolysis methods were conducted to evaluate the occurrence state and oil content of the P_{1f} shale in the Hashan area. The results indicate that plagioclase (average 30.7%) and quartz (24.1%) dominate the mineral compositions of the P_{1f} shale samples. A method involving quartz–plagioclase–carbonate minerals is proposed to conduct lithofacies classification. In the Hashan area, the organic matter abundance in the P_{1f} shale is scaled in fair to good range, the thermal maturity ranges from immature to early mature stage, and the primary organic matter types are Types I and II₁. Intergranular and dissolution pores are the two most common pore types. The free oil is mostly found in the pores and microfractures of the mineral matrix, whereas the adsorbed oil is mostly adsorbed on the surfaces of kerogen and clay minerals. The high organic matter abundance, quartz content, and porosity account for substantial increase in the oil content, the area rich in shale oil resources coincides with that rich in free oil. The most favorable lithofacies in the Hashan area is the calcareous mudstone/shale, which hosts the highest free oil content (average 2.49 mg), total oil content (15.02 mg/g), organic matter abundance (TOC = 1.88% and $S_1 + S_2 = 20.54$ mg/g) and porosity (5.97%).

Keywords: Hashan area; Oil content; Occurrence state; Pore types; T_1 – T_2 NMR; Shale oil

1. Introduction

Shale oil refers to the oil resources that accumulate in the pore space of tight shale reservoirs and has become an important hydrocarbon resource (Sonnenberg and Pramudito, 2009; Bai et al., 2020). The discovery of the Bakken shale oil in the United States has rendered the exploration and development of shale oil a hot topic (Liu et al.,

2017; Abarghani et al., 2020). Furthermore, shale oil is considered a viable alternative for unconventional oil, which could alleviate the energy shortage in China (Lu et al., 2016; Jin et al., 2021). Currently, the shale oil flow has been derived from the Paleogene Shahejie Formation in the Bohai Bay Basin (Chen et al., 2021), Triassic Yanchang Formation in the Ordos Basin (Yang et al., 2016b; Ju et al., 2020), and Permian Fengcheng Formation in the Junggar Basin in China (Wang et al., 2021b), demonstrating good prospects for hosting oil and gas resources.

The Junggar Basin is a large and petroliferous superimposed sedimentary basin in China. Recently, drilling and testing of the P₁f shale oil led to remarkable achievements (Zhi et al., 2019; Wang et al., 2021b). Mega oil field reserves have recently been discovered in the Mahu Sag (Yu et al., 2018), which holds great potential for both oil and gas exploration (Zhi et al., 2019; Tang et al., 2021). Located near the northwestern boundary of the Mahu Sag, the Hashan area (Fig. 1c; also called the Hala'alate Mountain) also got a great breakthrough in shale oil exploration in recent years. The reserve scale of several exploration wells of the Fengcheng Formation in the Hashan area estimates approximately 789 million tons, implying high potential for exploration activities. Owing to the combination of multiple tectonic movements and influence of volcanic activities (Li et al., 2021a), the tectonic evolution and oil content in the Hashan area shale differ from those in the Mahu Sag, posing numerous challenges to the shale oil exploration and development in the Hashan area (Yu et al., 2019; Cao et al., 2020). Determining the oil-bearing capacity of shale in the Hashan area is essential for optimizing exploration activities and evaluating the resource potential of shale oil in the northwestern margin of the Junggar Basin.

Fig. 1. (a) Location of the Junggar Basin in China; (b) Location of the Hashan area; (c) Location of

the Wells and contour map of the dark mudstone thickness of the P₁f; and (d) Profile of the stratigraphic distribution and fractures in the Hashan area.

Free, adsorbed, and dissolved states are considered the three occurrence states of shale oil in the shale reservoir (Li et al., 2018a, 2018b). The scanning electron microscopy (SEM) observations and nuclear magnetic resonance (NMR) T_1 – T_2 spectra are the two most commonly used experimental methods to distinguish the occurrence states of shale oil. The pore structures of the shale samples are clearly visible under the SEM after being hand-polished and argon-ion milled. However, this also leads to the loss of shale oil in the pores (Das et al., 2021). Therefore, to distinguish the occurrence state of shale oil in the pores, cores with different oil content were selected in this study. The fresh surface was knocked out and quickly placed in the sample chamber for direct SEM observations. The NMR T_1 – T_2 spectra, which is a nondestructive technique, can more clearly reveal different occurrence states in shales than SEM. Zhang et al. (2020) proposed the oil-bearing shale T_1 – T_2 pattern diagram, which efficiently segregates the contributions from the different compartments containing protons. Li et al. (2020) found a positive correlation between the intensity of NMR T_1 – T_2 spectra signals and the free and adsorbed oil contents from a modified multistage Rock-Eval method, and proved that NMR can be used to identify and quantify the adsorbed versus free oil contents. And this method was also used to systematically assess the in situ water and oil content, distribution, and their evaporative loss laws of preserved shales (Li et al., 2022b).

Oil content in shale refers to the amount of liquid hydrocarbon generated by kerogen and retained in shale after the hydrocarbon expulsion (Jarvie, 2012). The oil-bearing capacity of shale is largely associated with the free oil content in shale, which is also a concern for the appraisal of effective shale oil resources (Zhao et al., 2020; Wang et al., 2021a). The shale oil content in the P₁f shale in the Hashan area is accurately

characterized in this study based on the conventional and multistage Rock-Eval pyrolysis methods. The pyrolysis parameter S_1 (residual hydrocarbon) from conventional Rock-Eval pyrolysis is generally used as a key criterion for examining shale oil content (Lu et al., 2012; Zhang et al., 2022). However, multiple investigations have demonstrated that a small quantity of light and heavy oil is lost during sample collection, transportation, and storage before conducting the pyrolysis analysis. In this paper, the shale samples were collected from the core library and the sample pretreatment was carried out at room temperature. Thus, our study was based on the fact that light hydrocarbons were partly lost. Furthermore, another portion of heavy oil is not released during the pyrolysis, implying that the S_1 content is lower than the real oil content. Therefore, Jiang et al. (2016) proposed the multistage Rock-Eval method to further refine the conventional Rock-Eval pyrolysis experiments. The original S_1 and S_2 are precisely divided into four parts: S_{1-1} , S_{1-2} , S_{2-1} , and S_{2-2} . The main components of S_{1-1} , S_{1-2} , S_{2-1} , and S_{2-2} are light oil, light-medium oil, asphaltene and heavy oil, and hydrocarbons from the kerogen pyrolysis, respectively. This method is a good way to characterize the shale oil occurrence and quantitatively evaluate the shale oil resource, it also may reduce the impact of the frequency-occurred carryover effect to some extent (Zhang et al., 2020).

We conduct a case study covering the organic matter characteristics, pore types, shale oil occurrence states, and oil content evaluations using the petrological observations, SEM observations, 2D T_1 - T_2 NMR, and multistage Rock-Eval methods to examine the occurrence states and oil content in the P_1f shale in the Hashan area. This study is significant as it presents a pilot investigation of shale oil in the Hashan area.

2. Geological setting

The Junggar Basin is the second-largest petroliferous sedimentary basin in the

northwestern part of China, covering an area of $1.3 \times 10^5 \text{ km}^2$ (Luo et al., 2018; Chang et al., 2019). With coverage of 1000 km^2 , the Hashan area is located in the northwestern margin of the Junggar Basin (Fig. 1a–b). The northern part of the Hashan area is bounded by the Darbute fault and is adjacent to the Heshtologi Basin, whereas the southern part is close to the Wuxia fault belt (Fig. 1c). The Hashan area is a typical foreland thrust belt. The formation of the Hala'alate Mountain tectonic belt has been affected by the multistage tectonic movements during the Hercynian, Indosinian, Yanshan, and Himalayan periods (Li et al., 2018c), producing a strip shape in the plane. The belt appears as a large thrust nappe structure in the profile (Fig. 1d).

The Hala'alate Mountain was formed from a northern nappe generated by severe collisional forces and multistage volcanic activities during the Late Carboniferous–Early Permian (Wang et al., 2018). During the Late Triassic Indosinian period, large nappe and thrust faults reactivated, creating several new secondary faults. The Hala'alate Mountain was uplifted once more, and its shape was formed (Zhang et al., 2021b). Jurassic period onward, the tectonic activity weakened substantially, and the Jurassic and Cretaceous strata overlaid the Triassic or ancient nappe strata (Fig. 1d). The nappe structure zone in Fig. 1c corresponds to the position of the nappe structure.

The Carboniferous, Permian, Triassic, Jurassic, Cretaceous, Palaeogene, Neogene, and Quaternary strata form the stratum of the Hashan area from bottom to top. The lower P_{1f} lies above the Jiamuhe Formation and below the Xiazijie Formation (Fig. 2). The P_{1f} in the Hashan area is primarily composed of dark mudstone, tuff, conglomerates, sandstones, and dolomite. The Permian Fengcheng Formation developed a fan delta-lake sedimentary system, forming a large semi-closed or full-closed terrestrial saline lacustrine carbonate sedimentary environment accompanied by volcanic activities (Zhang et al., 2019; Zhang et al., 2021a). The volcanic eruptions were frequent and

tectonic activity was intensive during the Carboniferous–Permian transition, which resulted in the widespread distribution of volcanic and pyroclastic rocks (Yu et al., 2019). The P_{1f} was also considered as high-quality organic-rich source intervals which generated abundant hydrocarbon resources (Hu et al., 2017).

Fig. 2. Stratigraphic column of the Hashan area and cores from target wells of the P_{1f} .

3. Samples and experiments

A total of 67 shale core samples of the P_{1f} were collected from four wells in the Hashan area. The locations of the four wells are presented in **Fig. 1c**. A relatively complete experimental study was performed, covering the detection of the total organic carbon content (TOC), X-ray diffraction (XRD) analysis, conventional Rock-Eval pyrolysis, multistage Rock-Eval pyrolysis, thin-section observations, SEM observations, and T_1 – T_2 NMR experiments.

To conduct the Rock-Eval analysis, the shale core samples were crushed to 100 mesh. The Rock-Eval pyrolysis was performed using a Rock-Eval-VI instrument. S_1 was determined at a constant temperature of 300 °C for three minutes, and subsequently the temperature was raised to 600 °C at a rate of 25 °C/min to obtain S_2 . The multistage Rock-Eval method was modified by Jiang et al. (2016).

Thin-section observations were performed using a Leica DM2500 microscope equipped with light-emitting diode illumination and digital camera detection system of LAS V4.2. The goal of the thin-section observations is to confirm the mineral constituents and lithologic characteristics of the core samples.

A Phenom prox scanning electron microscope was employed to conduct the SEM tests. The SEM was used to examine 32 samples from the four wells in this study. To verify the pore structure of shale, several samples were cut parallel to the bedding

surface and mounted on stubs and were then hand-polished. Subsequently, a flat surface was obtained through argon-ion milling. To observe the shale oil occurrence state, several samples were sliced into pieces and not polished, allowing the newly exposed pore surface to be clearly observed under the SEM. Energy dispersive spectrometry (EDS) is a common analytical technique used for elemental analysis. In this study, the EDS was employed for analyzing the energy spectral composition of oil in shales.

The T_1 – T_2 NMR experiments were conducted using a Niumag (China) MicroMR23-060H-1 instrument, whose magnetic field strength measures 0.5 T at a frequency of 21.36 MHz, and which was operated at 32 °C. The following were the NMR parameters: echo spacing (TE) of 0.07 ms, inverse times of 61, waiting time (TW) of 1000 ms, maximum echo numbers of 6000, and scanning numbers of 32. All as-received samples used for T_1 – T_2 map measurements were core fragments whose weight ranged from 9.47 to 65.30 g.

4. Results and discussion

4.1 Petrological characteristics and lithofacies classification

XRD analysis indicates that the samples comprise quartz (up to 71.6%; average 24.1%), orthoclase (1.3%–35.6%; average 4.8%), plagioclase (4.1%–63.8%; average 30.7%), calcite (up to 57.2%; average 9.0%), dolomite (2.7%–49.5%; average 12.8%), clay minerals (up to 45.3%; average 15.5%), and small amounts of pyrite and amphibolite (**Table 1**). Plagioclase demonstrates the greatest average content among all minerals. The mineral composition of the P_{1f} is dominated by felsic minerals (quartz, orthoclase, and plagioclase), with fewer carbonate minerals (calcite and dolomite) and clay minerals, compared to shales from the Dongying Depression and Jiangnan Basin (**Fig. 3a**). Therefore, the carbonate–felsic–clay mineral lithofacies classification commonly used in other areas (Li et al., 2021a; Liu et al., 2021) does not apply to the

Hashan area.

Table 1 Mineral composition of the Pdf shale in the Hashan area.

Well	Depth (m)	Quartz (%)	Orthoclase (%)	Plagioclase (%)	Calcite (%)	Dolomite (%)	Amphibolite (%)	Clay (%)	Pyrite (%)
HQ6-1	1562	23.4	8.1	10.8	22.6	3.8	0.0	28.8	2.5
HQ6-2	1562.5	22.4	4.5	0.0	21.5	3.9	0.0	45.3	2.3
HQ6-3	1563.5	25.4	5.9	21.5	10.8	0.0	0.0	33.3	3.0
HQ6-5	1918.6	44.8	3.5	6.5	12.8	0.0	0.0	30.8	1.6
HQ6-6	1918.65	18.4	5.2	35.8	18.0	0.0	0.0	21.3	1.2
HQ6-7	1920.55	17.3	5.2	35.3	17.9	0.0	0.0	22.8	1.5
HQ6-8	2539.4	7.6	4.6	58.1	4.4	7.0	0.0	15.5	2.8
HQ6-9	2539.9	24.6	1.5	16.3	0.0	29.6	0.0	26.2	1.9
HQ6-10	2540.2	38.4	2.0	32.6	0.0	15.8	0.0	9.7	1.6
HQ6-11	2540.59	21.8	3.6	13.5	0.0	18.0	0.0	41.3	1.8
HQ6-12	2541.405	28.3	2.4	21.8	0.0	24.8	1.3	19.4	2.0
HQ6-13	2541.63	21.3	4.1	22.2	0.0	30.1	0.0	20.3	1.9
HQ6-14	2544.645	24.0	3.6	28.2	0.0	20.3	2.4	19.0	2.4
HQ6-15	2544.645	22.1	1.3	9.5	0.0	39.4	0.0	26.4	1.3
HQ6-16	2545.5	28.9	0.0	19.8	0.0	19.8	0.0	29.1	2.4
HQ6-17	2598.325	13.3	4.8	52.8	4.5	2.9	0.0	19.5	2.3
HQ6-18	2697.425	22.5	5.7	29.3	0.0	19.4	0.0	20.3	2.8
HQ6-19	2698.305	10.9	9.8	41.5	0.0	22.9	2.3	9.9	2.6
HQ6-20	2699.5	6.0	2.3	18.2	0.0	49.5	0.0	21.0	3.0
HS1-2	2098.3	10.3	4.1	29.5	16.0	7.1	0.0	30.1	3.0
HS1-3	2098.38	19.8	7.7	34.8	17.8	6.8	0.0	11.1	2.0
HS1-4	2099.2	13.8	5.6	24.4	20.2	15.7	0.0	16.6	3.7
HS1-5	2099.93	13.7	6.6	35.7	19.3	12.7	0.0	9.2	2.7
HS1-6	2100.4	26.2	3.7	21.4	18.3	13.1	0.0	13.6	3.6
HS1-7	2100.73	25.6	11.9	33.8	7.1	3.8	0.0	14.0	3.8
HS1-8	2101.38	19.5	6.5	38.0	5.2	10.5	0.6	16.3	3.4
HS1-10	2103.1	27.1	5.3	32.8	9.0	11.7	0.0	11.6	2.4
HS1-11	2151.45	18.3	7.4	49.5	7.3	4.3	3.2	8.0	2.1
HS1-12	2152	32.1	4.1	21.0	12.6	18.5	0.0	9.5	2.2
HS1-13	2153.56	17.5	4.1	35.8	15.1	12.8	0.0	13.0	1.7
HS1-14	2154.67	13.8	3.5	20.7	18.4	13.1	0.0	27.2	3.4
HS1-15	2155.36	17.3	5.4	49.8	6.4	5.6	0.0	12.4	3.1
HS1-16	2156.2	28.9	2.0	9.6	3.6	46.9	0.0	7.9	1.1
HS1-17	2156.75	26.1	4.6	31.2	10.6	0.0	0.0	22.7	4.9
HSX1-1	3345.1	51.5	0.0	13.5	17.6	0.0	0.0	14.3	3.1
HSX1-2	3345.5	43.7	0.0	12.4	21.2	0.0	0.0	19.4	3.3
HSX1-3	3347.13	29.8	5.9	25.7	13.2	0.0	0.0	22.2	3.1
HSX1-4	3347	36.8	4.8	15.6	18.5	0.0	0.0	19.6	4.8

HSX1-5	3348.43	44.4	3.3	19.0	10.1	0.0	0.0	18.7	4.5
HSX1-6	3348.9	5.6	3.3	11.2	57.2	0.0	0.0	19.8	2.9
HSX1-7	3424.22	51.1	0.0	13.2	24.2	0.0	0.0	7.9	3.6
HSX1-8	3349.55	71.6	1.6	4.1	11.3	0.0	0.0	10.3	1.2
HSX1-9	3350.55	48.4	1.5	7.6	9.8	0.0	0.0	29.9	2.8
HSX1-10	3351.04	54.3	0.7	11.3	7.0	0.0	0.0	24.1	2.7
HSX1-11	3350.85	41.9	2.7	22.1	13.1	0.0	0.0	18.2	2.1
HSX1-12	3352.22	38.9	5.1	28.0	11.2	0.0	0.0	13.7	3.1
HSX1-13	3352.44	46.9	5.2	14.4	15.3	0.0	0.0	15.3	2.9
HSX1-14	3682.1	35.9	7.2	25.3	0.0	25.1	0.0	0.0	6.6
HSX1-15	3683.06	12.0	3.7	52.3	2.6	19.4	0.0	7.4	2.6
HSX1-16	3683.8	0.0	2.5	37.2	19.7	11.9	0.0	26.2	2.5
HSX1-17	3684.18	10.9	5.2	50.3	0.0	10.4	0.0	21.5	1.8
HSX1-18	3942.2	6.0	3.0	63.8	1.6	22.8	0.0	0.0	2.8
HSX1-19	3942.26	7.7	3.0	12.7	23.7	42.1	10.0	0.0	0.8
HS11-1	3922.36	1.6	35.6	28.1	19.6	2.7	4.4	6.8	1.1
HS11-2	3926.15	14.1	5.3	38.1	1.3	36.8	0.9	2.7	0.9
HS11-3	3927.1	31.4	7.2	43.1	5.3	9.0	3.6	0.0	0.4
HS11-4	3927.4	19.8	8.5	60.7	0.0	10.4	0.0	0.0	0.7
HS11-5	3927.6	17.6	2.6	40.8	0.0	34.9	0.9	2.5	0.8
HS11-6	3928.1	10.8	0.0	46.8	0.0	31.9	0.5	7.5	2.6
HS11-7	3928.45	30.0	5.9	49.9	0.0	7.2	1.2	4.2	1.6
HS11-8	3928.9	27.3	5.7	57.3	1.0	4.0	1.0	2.9	0.8
HS11-9	3929.68	7.3	7.8	51.3	0.0	27.5	1.6	3.2	1.2
HS11-10	3930.86	25.9	3.1	58.8	0.4	6.5	0.9	2.0	2.6
HS11-11	3931.61	25.9	11.1	37.3	0.0	12.8	1.6	7.9	3.5
HS11-12	3932.0	11.6	7.3	51.8	0.0	11.0	3.3	12.5	2.4
HS11-13	3932.61	8.8	4.8	50.2	0.0	28.3	0.5	4.8	2.7
HS11-14	3933.4	17.5	4.2	60.3	0.0	7.0	0.7	6.7	3.6
HS11-15	3933.9	18.0	1.3	44.9	0.0	21.0	1.3	10.0	3.5

Fig. 3. Ternary diagram of (a) a conventional lithofacies classification and (b) a new lithofacies classification of the P_{1f} in the Hashan area.

Extant literature showed that a considerable tuff was found in the P_{1f} stratum in the Hashan area (Li et al., 2018c; Yu et al., 2019). Tuff is usually made of volcanic ash and pyroclastic material with grain sizes less than 2 mm under the core observation and microscopic thin-section analysis (Wang et al., 2018). The primary component of the pyroclastic material is mineral fragments characterized by sharp angles, smooth

surfaces, and a lack of secondary alteration minerals. Plagioclase is the major mineral that forms the mineral fragments according to the XRD analysis. Therefore, in this study, plagioclase is selected as a prominent member of lithofacies classification to represent tuff. Consequently, the following three end-member lithofacies classification: quartz–plagioclase–carbonate mineral is proposed (**Fig. 3b**).

For the P_{1f} samples, when the grain size of most minerals exceeds 10 μm and the mineral composition is dominated by quartz and feldspar, the rocks are classified as argillaceous siltstone; when the grain size of most minerals is less than 10 μm , the rocks are classified as fine-grained. Fine-grained rocks are classified as shale/mudstone when they are predominantly formed of quartz and orthoclase, and they are further categorized into tuffaceous, calcareous, and dolomitic shales/mudstones depending on the main component of the remaining minerals. Shale and mudstone are classified by the presence of laminae under a microscope. Based on the main carbonate mineral, the rocks are categorized into dolomite or limestone when the content of dolomite or limestone exceeds 40%. The rocks are classified as tuff when the plagioclase content surpasses 50%, and they are further categorized into dolomitic and calcareous tuffs based on the major component of the remaining minerals.

The rocks in the P_{1f} can be classified into four primary types and seven subtypes. The typical characteristics of the particular lithofacies are illustrated in **Fig. 4**. Quartz and calcite account for the largest content of minerals in the calcareous mudstone/shale, which also host certain amounts of plagioclase. Mineral grain sizes range between 40 and 100 μm , with well-developed laminae, according to microscopic examination. Numerous fractures are developed, which are filled with quartz and calcite as well as spindle-shaped dissolution pores. The mineral composition of dolomitic mudstone/shale is dominated by dolomite, followed by quartz and clay minerals. Under

the microscope, the grain size of the minerals ranges from 20 to 130 μm , with no laminae or fractures visible. Dolomite in the dolomitic mudstone/shale has a small grain size and narrower dispersion. Several dissolution pores are filled with quartz. Quartz and clay minerals dominate the mineral composition of tuffaceous shale, followed by plagioclase. The microscopy analysis revealed that mineral grain sizes ranged from 40 to 100 μm , showing a granular structure with no fractures or dissolution pores. The mineral composition of dolomitic tuff is dominated by plagioclase and dolomite. The minerals have a granular structure and do not contain laminae, with grain sizes ranging from 20 to 80 μm . Dolomite aggregates, and a few fractures are developed. Dolomite dominates the mineral composition of tuff-bearing dolomite. The microscopy analysis reveals a considerable number of granite debris. The granite debris is composed of orthoclase, plagioclase, and quartz, whereas the lamina is relatively developed. The argillaceous siltstone is mainly composed of plagioclase, followed by clay minerals and calcite. The argillaceous siltstone has a granular structure without laminae or fractures, with grain sizes ranging from 100 to 200 μm .

Fig. 4. Basic features of the different lithofacies of the P_{1f} in the Hashan area.

4.2 Organic geochemical characteristics

The TOC and hydrocarbon generation potential ($S_1 + S_2$) are two commonly used indicators for evaluating the organic matter abundance in source rocks (Tissot and Welte, 1984). The TOC values of the P_{1f} samples range from 0.12% to 5.13% (average 1.17%), with the majority being less than 2%. The $S_1 + S_2$ values range from 0.02 mg/g to 54.36 mg/g (average 8.58 mg/g), most of which are less than 20 mg/g. These data indicate that most core samples of the P_{1f} are abundant in organic matter and have fair to good petroleum generation potential (Peters and Cassa, 1994). Among all lithofacies, the

calcareous mudstone/shale contains the highest TOC values (average 1.88%; **Fig. 5a**) and the highest $S_1 + S_2$ values (average 20.54 mg/g; **Fig. 5b**). Only the calcareous mudstone/shale exceeds the TOC and $S_1 + S_2$ values of the tuffaceous mudstone/shale and calcareous tuff. The siltstone lithofacies hosts the lowest organic matter abundance.

Fig. 5. Total organic carbon content (TOC) (a) and hydrocarbon generation potential ($S_1 + S_2$) (b) of samples in different lithofacies.

According to the hydrogen index–temperature maximum (HI– T_{max}) chart, the organic matter type of the Fengcheng Formation samples tends to be sapropelic (Type I) and humic-sapropelic (Type II₁). Both types have significant implications for oil generation capacity (**Fig. 6a**; Tissot and Welte, 1984; Hakimi et al., 2012). The types of organic matter differ depending on the lithofacies: the organic matter types in mudstone/shale are similar, mostly Type I and Type II₁, with the calcareous mudstone/shale being the best. The main organic matter types in the dolomitic tuff and argillaceous siltstone, with poor oil generation capacity, are Types II₂ and III.

Fig. 6. Organic matter types (a) and thermal maturity (b) assessment of the P_{1f} samples in the Hashan area.

The T_{max} serves as an excellent parameter to represent thermal maturity. The T_{max} values of the P_{1f} samples vary from 410 to 447 °C, with an average of 421 °C, indicating that the thermal stage of organic matter is characterized immature–early mature. The sterane isomerization index is another good indicator of thermal maturity (Peters et al., 2005; Lerch et al., 2016). The C₂₉ sterane $a\beta\beta/(aaa + a\beta\beta)$ ratios for 14 samples from the P_{1f} range between 0.217 and 0.379. The C₂₉ sterane 20S/(20S + 20R) ratios range between 0.103 and 0.390 (**Fig. 6b**), which also imply that the thermal state of organic matter has reached an early mature stage.

4.3 Pore types and porosity

Based on the classification made from Loucks et al. (2012), the pores can be divided into four primary types: (1) organic-matter pores, (2) intraparticle pores, including dissolution, cleavage, and intercrystalline pores, (3) interparticle pores, and (4) fracture pores.

The organic-matter pores are formed by the organic matter during the thermal cracking and hydrocarbon generation and are mainly developed in the kerogen masses (Loucks et al., 2009) with elliptical or round shapes (Fig. 7a). Only a few organic-matter pores have been discovered in the calcareous shale/mudstone, demonstrating higher organic matter abundance than other lithofacies. The intraparticle pores in the clay minerals are mostly developed between the crystals of the clay particles, with shapes varying from sheet-like to triangular (Fig. 7b and I). The cleavage pores in the orthoclase were formed by the rupture of orthoclase along the cleavage plane, which is only found in the calcareous shale/mudstone and displays a plate-like shape (Fig. 7e). The pyrite intercrystalline pores are commonly found in the pyrite framboids, whereas the pore shapes are relatively regular and display a polygonal or triangular shape (Loucks et al., 2012; Fig. 7f). The dissolution pores are formed by the mineral dissolution during diagenesis. Their pore shapes are mostly regular and round, and they may occur in quartz, calcite, dolomite, and other mineral grains (Fig. 7c–d). In tuff-bearing dolomite, a considerable number of dissolution pores exist, demonstrating that the carbonate minerals are susceptible to diagenetic alteration and play an important role in improving the physical properties of the shale reservoirs (Zhang et al., 2018b). With different shapes and sizes, the interparticle pores between different mineral particles usually have good connectivity and constitute effective seepage channels of shale (Loucks et al., 2012). The interparticle pores between the carbonate minerals and

orthoclase usually present regular polygons, (**Fig. 7 h–i**), whereas the morphology of interparticle pores between quartz is more complex, varying from elongated to meniscus (**Fig. 7g and k**). The calcareous, tuffaceous, and dolomitic shales/mudstones have high quartz content and are dominated by interparticle pores between quartz. The fracture pores that are found in the tuff-bearing dolomite are mostly distributed in strips, which can cut through mineral particles to form effective shale seepage channels (**Fig. 7j**).

Fig. 7. Pore types identification from the SEM images of the samples in the Hashan area.

Shale oil is found mostly in the shale pore space. Porosity largely helps determine the size of the pore space. The high porosity of shale suggests that numerous pores were developed and a huge pore space was formed, which is advantageous to the enrichment of shale oil (Li et al., 2019). The NMR T_2 spectrum calculation indicates that the porosity of different lithofacies greatly differs (**Fig. 8**). The porosity of the calcareous mudstone/shale is the highest (average 5.97%), followed by the dolomitic mudstone/shale (2.95%).

Fig. 8. Porosity of different lithofacies in the Hahsan area.

4.4 Shale oil occurrence states

The energy spectral composition analysis results (**Fig. 9 d–f, j–l**) demonstrate high concentration percentage of carbon, which obviously indicates the presence of oil in the shale. Furthermore, the SEM images demonstrate that shale oils are present in the shale reservoirs of the P_{1f} and are mostly found in the free and adsorbed states. The free oils are found primarily in large fractures and pores (**Fig. 9 a–c**) and take the form of irregular oil films with black color. The adsorbed oils are mostly found disseminated on the surface of pyrite aggregates and clay minerals (**Fig. 9 g–i**), and they have a gray

color and blurry boundary with the surrounding minerals (Li et al., 2022a).

Fig. 9. Shale oil occurrence states from the SEM images of samples in the Hashan area. (Conc. = concentration percentage).

The T_1 – T_2 NMR experiment is an effective way of determining the occurrence states of shale oil (Zhang et al., 2020). The NMR T_1 – T_2 spectrum of Sample HS11-10, a dolomitic tuff with S_1 content of 0.57 mg/g and clay mineral content of 3.23%, are illustrated in **Fig. 10f**. On the T_1 – T_2 spectrum, four signal regions were identified according to Zhang's classification method: Region A represents clay mineral bound water, Regions B and C represent adsorbed and free oils, respectively, and Region D represents shale pore water. Among them, the signal of clay mineral bound water is characterized by a low T_2 peak at approximately 0.12 ms, and the center is located on the line $T_1/T_2 \sim 10$. The signal of the adsorbed oil is $0.2 \text{ ms} < T_2 < 2 \text{ ms}$ and is located near the line $T_1/T_2 \sim 100$. The signal of the free oil is with a $T_2 > 2 \text{ ms}$ and is located close to the line $T_1/T_2 \sim 10$. The center of the shale pore water is located close to the line $T_1/T_2 \sim 1$, and the T_2 peak is approximately 0.5 ms.

Fig. 10. NMR T_1 – T_2 spectra of shale in original states. (A = clay mineral bound water; B = Adsorbed oil; C = Free oil; D = shale pore water.)

The NMR T_1 – T_2 spectra differ depending on lithofacies, which are mainly affected by clay mineral bound water. The higher the clay mineral content is, the higher the clay mineral bound water content is and the stronger the signal of bound water on the T_1 – T_2 spectrum is. These result in a relatively weak irreducible oil signal. Taking HQ6-8 and HSX1-11 as examples, HQ6-8 (**Fig. 10a**) is an argillaceous siltstone with low bound water content and low S_1 content (0.61 mg/g), whereas the irreducible oil signal is relatively high, rendering the free oil signal clearly visible on the T_1 – T_2 spectrum.

HSX1-11 (**Fig. 10b**) demonstrates a calcareous shale with high bound water and S_1 content (4.02 mg/g), whereas the irreducible oil signal is relatively weak, rendering the free and adsorbed oils signal too weak to be identified on the T_1 – T_2 spectrum.

The contents of adsorbed and free oils vary in shale with diverse lithofacies, according to the NMR T_1 – T_2 spectrum of the original shale. The irreducible oil of the argillaceous siltstone is dominated by the free oil (**Fig. 10a**). The calcareous mudstone/shale has a high total oil content. However, the irreducible oil is mainly composed of the adsorbed oil with less free oil (**Fig. 10b**). The adsorbed oil dominates the dolomitic mudstone/shale, with a reasonably high proportion of the adsorbed oil and just a small amount of the free oil (**Fig. 10c**). The irreducible oil content of the tuffaceous mudstone/shale and calcareous tuff is low ($S_1 < 0.3$ mg/g), demonstrating a poor oil-bearing capacity, whereas the signal of the irreducible oil on the T_1 – T_2 spectrum is weak (**Fig. 10d–e**). The dolomitic tuff has a reasonably high free oil content, but a low total oil content (**Fig. 10f–g**). The irreducible oil of the tuff-bearing dolomite is dominated by the free oil (**Fig. 10 h–i**).

4.5 Shale oil content

The S_1 content in various lithofacies are depicted in **Fig. 11a**. Compared with other lithofacies, the calcareous mudstone/shale demonstrates the highest S_1 content, with a mean value of 1.26 mg/g, indicating a high oil content. The dolomitic mudstone/shale has a slightly lower oil content than the calcareous mudstone/shale, with S_1 content ranging from 0.13 to 2.26 mg/g and a mean value of 0.56 mg/g. The S_1 content in the remaining five lithofacies are less than 2 mg/g, with average values less than 0.5 mg/g.

Fig. 11. (a) S_1 and (b) S_1 /TOC of samples in different lithofacies.

Jarvie (2012) proposed an oil saturation index ($OSI = S_1/TOC \times 100$) that could serve

as a favorable evaluation index for the shale oil exploration. A higher OSI means higher oil mobility and a higher amount of potentially producible petroleum. The calcareous mudstone/shale demonstrates the highest OSI value (**Fig. 11b**), denoting the highest oil mobility of all lithofacies. Furthermore, the argillaceous siltstone and dolomitic tuff have high OSI values, demonstrating high oil mobility.

The multistage Rock-Eval method is a further refinement of the conventional Rock-Eval pyrolysis method. The total content of S_{1-1} and S_{1-2} can be used to reflect the amount of free oil in shale; S_{2-1} primarily represents the adsorbed oil, and S_{2-2} primarily stands for the hydrocarbon regeneration potential of kerogen. The total oil content in shale can be calculated by adding S_{1-1} , S_{1-2} , and S_{2-1} .

The light oil (S_{1-1}) content of the P_{1f} shale samples in the Hashan area generally demonstrates low values (average 0.11 mg/g; **Fig. 12**), probably owing to the light oil lost during core sample collection, transportation, and storage. The light–medium oil (S_{1-2}) is the dominant component of the free oil ($S_{1-1} + S_{1-2}$). The free oil content varies substantially among lithofacies. The free oil content in the calcareous mudstone/shale is the highest (average 2.49 mg/g), whereas in the dolomitic mudstone/shale ranks the second (1.66 mg/g) among all lithofacies, which is consistent with the S_1 content result obtained from the Rock-Eval pyrolysis method. The free oil content in the tuff-bearing dolomite (0.49 mg/g) and calcareous tuff (0.45 mg/g) demonstrate the lowest values. Among all lithofacies, the calcareous mudstone/shale (average 12.53 mg/g) hosts the highest adsorbed oil content (S_{2-1}), whereas the argillaceous siltstone hosts the lowest one (average 1.13 mg/g). The adsorbed oil is the dominant component of the total oil amount. The calcareous samples (such as the calcareous mudstone/shale and tuff) and mudstone/shale (such as dolomitic and tuffaceous mudstones/shales) generally have high oil-bearing capacity.

Fig. 12. Oil content of samples in different lithofacies.

(A: argillaceous siltstone; B: calcareous mudstone/shale; C: tuffaceous mudstone/shale; D: dolomitic mudstone/shale; E: dolomitic tuff; F: calcareous tuff; and G: tuff-bearing dolomite.)

The total oil content demonstrates a good linear relationship to the free oil/adsorbed oil content (**Fig. 13 a–b**). The higher the total oil content is, the higher the adsorbed and free oils content are, indicating that the area rich in the shale oil resources coincides with the area rich in the free oil.

Fig. 13. Relationships between the total oil content and (a) free oil content (b) adsorbed oil content.

4.6 Main controlling factors of oil content

4.6.1 Organic matter characteristics

Lu et al. (2012) proposed the classification and evaluation criteria for the shale oil and gas resources to accurately examine the resource potential of shale oil and gas. **Fig. 14a** classifies the P₁f shale oil into three levels of resources on the basis of enrichment degree: ineffective, low efficient, and enriched resources. The ineffective resources are considered to have both poor oil-bearing potential and low oil contents (TOC < 1% and S₁ < 0.5 mg/g). The low efficient resources are characterized by medium oil-bearing potential and medium oil contents (1% < TOC < 2% and 0.5 mg/g < S₁ < 1.5 mg/g). The enriched resources demonstrate the greatest oil-bearing potential and high oil contents (TOC ≥ 2% and S₁ > 1.5 mg/g).

Fig. 14. Relationships between (a) TOC and S₁, (b) TOC and free oil content, (c) TOC and adsorbed oil content of samples in the Hashan area. (d) The bubble-color chart of quartz–calcite–oil content of samples in the Hashan area. (The oil content is represented by the size of the bubble.)

There is a clear correlation between shale oil and TOC contents, namely, the amount

of the adsorbed oil is mainly affected by the abundance of organic matter. The higher the abundance of organic matter (TOC) is, the higher the amount of adsorbed oil is (**Fig. 14c**). The free oil content is divided into three stages as the TOC value rises (**Fig. 14b**). When TOC is less than 1%, the free oil is in a stable, low value (0.5 mg/g). When the TOC ranges between 1% and 2%, the free oil content gradually increases as the TOC content increases. When the TOC exceeds 2%, the free oil content enters a plateau stage, basically distributed above 2.0 mg/g, which is favorable to the enrichment of the P_{1f} shale oil.

4.6.2 Lithofacies and mineral composition

Minerals are the crucial components of shale and the primary places denoting the occurrence of shale oil. The influence of mineral composition on the oil enrichment can be elucidated by investigating the correlation between the major mineral composition and oil content of shale. The total oil content in the P_{1f} shale rises as the quartz and calcite content rises (**Fig. 14d**). However, it has a poor correlation with other components. Quartz and calcite minerals are beneficial for enriching oil. Since quartz is the main brittle mineral, an increase in its content favors the development of the shale pore throat (Yang et al., 2016a; Zhang et al., 2018a). Calcite is the main carbonate mineral, where organic acids released during the hydrocarbon generation process of the shale samples can easily form several dissolution pores (Yang et al., 2016a). The combined effect of the aforementioned two minerals increases the shale storage space and enhances the oil storage capacity. The oil content is represented by the size of the bubble in **Fig. 14d**. A larger bubble represents higher oil content. The P_{1f} shale demonstrates the highest oil content when the quartz content reaches 35% and the calcite content exceeds 10%, which corresponds exactly to the calcareous mudstone/shale.

In terms of the most valuable lithofacies of the P_{1f} samples (**Fig. 15**), the calcareous mudstone/shale demonstrates the highest organic matter abundance (TOC = 1.88% on average, $S_1 + S_2 = 20.54$ mg/g on average), is conducive to shale oil generation and enrichment. The organic matter types in the calcareous mudstone/shale are Types I and II_1 , which have significant implications for oil generation. The mineral composition of the calcareous mudstone/shale is dominated by quartz (average 39.6%) and calcite (18.58%), and the calcite strips are laminated, with numerous fractures. The calcareous mudstone/shale demonstrates the highest total oil (average 15.02 mg/g) and free oil (average 2.49 mg/g) contents besides the highest oil mobility. Furthermore, the dolomitic mudstone/shale (TOC = 1.27%, $S_1 + S_2 = 6.80$ mg/g) and tuffaceous mudstone/shale (TOC = 1.64%, $S_1 + S_2 = 9.86$ mg/g) have high organic matter abundance, the primary organic matter types are Types I and II_1 . Quartz and dolomite dominate the mineral composition of the dolomitic mudstone/shale, whereas quartz and plagioclase dominate the mineral composition of the tuffaceous mudstone/shale. The total oil and free oil contents in the dolomitic mudstone/shale (6.99 and 1.66 mg/g, respectively), and the tuffaceous mudstone/shale (7.55 and 1.21 mg/g, respectively) are lower than those in the calcareous mudstone/shale. With the lowest total oil content (1.93 mg/g), the argillaceous siltstone has the largest grain size and hosts the lowest organic matter abundance (TOC = 0.31%, $S_1 + S_2 = 1.21$ mg/g) among all lithofacies. The predominant organic matter types are Types II and III. The mineral composition is dominated by plagioclase and clay minerals.

Fig. 15. Primary controlling factors of the shale oil enrichment of samples in the Hashan area.

4.6.3 Pore structures

The porosity curve demonstrates a consistent trend with the total oil content curve

(**Fig. 15**), indicating that the porosity, together with the organic matter abundance and mineral composition, strongly affect oil content. Meanwhile, the pore types of the calcareous mudstone/shale and dolomitic mudstone/shale are dominated by the dissolution and interparticle pores between quartz. Considering the high carbonate minerals and quartz content in these two lithofacies, we show that the presence of carbonate minerals improves the reservoir's physical properties and that the high quartz content in shale favors the development of larger pore throats (Ross and Bustin, 2009). These combined impacts enhance the pore space, is beneficial to the shale oil enrichment (Hu, et al., 2021).

4.6.4 The nappe structure

The Hashan area is a large thrust nappe superimposed system developed gradually from the late Paleozoic. Wells HQ6 and HS1 are in the position of nappe structure, while wells HSX1 and HS11 are in the position of parautochthone (**Fig. 1c**). In comparison to wells HQ6 and HS1, wells HSX1 and HS11 have greater average total oil content ($7.632 \text{ mg/g} > 4.056 \text{ mg/g}$). The mineral composition of wells in the nappe and parautochthone differs due to the stratigraphic deposition difference. The samples from wells HSX1 and HS11 contain more carbonate minerals (calcite/dolomite) than wells HQ6 and HS1 (**Table 1**). As mentioned in section 4.6.3, the presence of carbonate minerals can enhance the pore space and favor the reservoir's physical properties. Therefore, the control of the nappe structure on oil content is indirect and is reflected in the mineral composition and pore structure.

In the P_{1f} , the main factors affecting the shale oil content are summarized (**Fig. 15**). There is a relationship between organic matter and oil contents; when the organic matter types are Types I and II_1 (which have significant implications for oil generation capacities), the higher the organic matter abundance and thermal maturity are, the more

conducive to the increase in oil content is. The influence of mineral composition on oil content is that the higher the content of quartz and carbonate minerals is, the more favorable to shale oil enrichment is. The calcareous mudstone/shale and dolomitic mudstone/shale are favorable lithofacies in the study area, whereas the argillaceous siltstone hosts the lowest oil content among all lithofacies. There is a relationship between the shale pores and oil content: high porosity increases oil content and the existence of numerous dissolution pores and intergranular pores increases the pore space and improves the reservoir's physical properties. Therefore, we conclude that the intervals hosting high shale oil content are characterized by high porosity, and high abundance of organic matter and quartz content.

5. Conclusions

A three-end method involving the use of quartz–plagioclase–carbonate minerals is proposed as a new lithofacies classification for determining the complex mineral composition of the P_{1f} shales in the Hashan area. Seven basic lithofacies were recognized. The organic matter abundance of the P_{1f} in the Hashan area is in fair to good range ($0.12\% < \text{TOC} < 5.13\%$, 1.17% on average; $0.02 \text{ mg/g} < S_1 + S_2 < 54.36 \text{ mg/g}$, 8.58 mg/g on average). The thermal stage is characterized immature–early mature. The most common organic matter types are Types I and II_1 , both of which have good oil generation ability. The main pore types include the intergranular and dissolution pores, which are conducive to oil and gas reservoirs. The free oil is mostly found in the pores and microfractures of the mineral matrix, whereas the adsorbed oil is mostly adsorbed on the surfaces of kerogen and clay minerals. The high organic matter abundance, high quartz content, and high porosity largely contribute to the increase in oil content.

The most favorable lithofacies in the study area is the calcareous mudstone/shale,

which hosts the highest S_1 (1.26 mg/g) and total oil content (average 15.02 mg/g), demonstrating the highest porosity (average 5.97%) and the highest organic matter abundance (TOC = 1.88% and $S_1 + S_2 = 20.54$ mg/g) and quartz (39.6%) contents.

Acknowledgments

This study was co-funded by the National Natural Science Foundation of China (Grant No. 42072172, 41772120), Shandong Province Natural Science Fund for Distinguished Young Scholars (Grant No. JQ201311) and the Graduate Scientific and Technological Innovation Project Financially Supported by Shandong University of Science and Technology (Grant No. YC20210825). We thank the Shengli Oil Company of Sinopec for approving the publication. We also acknowledge the experts of Elsevier Webshop Support for its linguistic assistance during the preparation of this manuscript. We thank four anonymous reviewers for their constructive reviews.

References

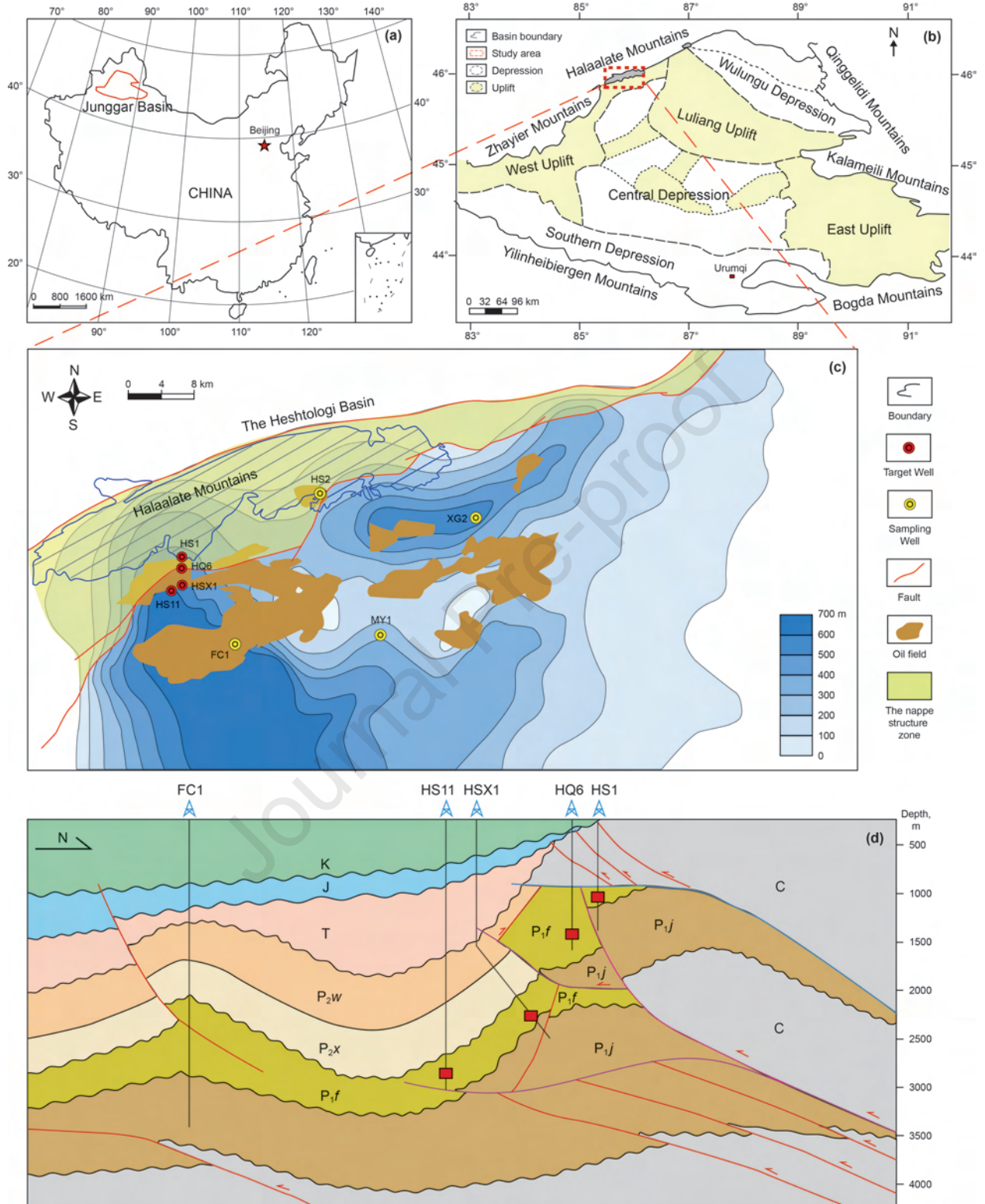
- Abarghani, A., Gentzis, T., Liu, B., et al., 2020. Preliminary investigation of the effects of thermal maturity on redox-sensitive trace metal concentration in the Bakken source rock, North Dakota, USA. *ACS Omega* 5, 7135–7148. <https://doi.org/10.1021/acsomega.9b03467>.
- Bai, C.Y., Yu, B.S., Han, S.J., et al., 2020. Characterization of lithofacies in shale oil reservoirs of a lacustrine basin in eastern China: Implications for oil accumulation. *J. Petrol. Sci. Eng.* 195, 107907. <https://doi.org/10.1016/j.petrol.2020.107907>.
- Cao, J., Xia, L.W., Wang, T.T., et al., 2020. An alkaline lake in the Late Paleozoic Ice Age (LPIA): A review and new insights into paleoenvironment and petroleum geology. *Earth Sci. Rev.* 202, 103091. <https://doi.org/10.1016/j.earscirev.2020.103091>.
- Chang, X.C., Wang, Y., Shi, B.B., et al., 2019. Charging of Carboniferous volcanic reservoirs in the eastern Chepaizi uplift, Junggar Basin (northwestern China) constrained by oil geochemistry and fluid inclusion. *AAPG Bull.* 103(7), 1625–1652. <https://doi.org/10.1306/12171818041>.
- Chen, D., Pang, X.P., Li, L., et al., 2021. Organic geochemical characteristics and shale oil potential of the middle Eocene early-mature shale in the Nanpu Sag, Bohai Bay Basin, eastern China. *Mar. Petrol. Geol.* 133, 105248. <https://doi.org/10.1016/j.marpetgeo.2021.105248>.
- Das, D., Mishra, B., Gupta, N., 2021. Understanding the influence of petrographic parameters on strength of differently sized shale specimens using XRD and SEM. *Int. J. Min. Sci. Technol.* 31(5), 953–961. <https://doi.org/10.1016/j.ijmst.2021.07.004>.
- Hakimi, M.H., Abdulah, W.H., Shalaby, M.R., 2012. Geochemical and petrographic characterization

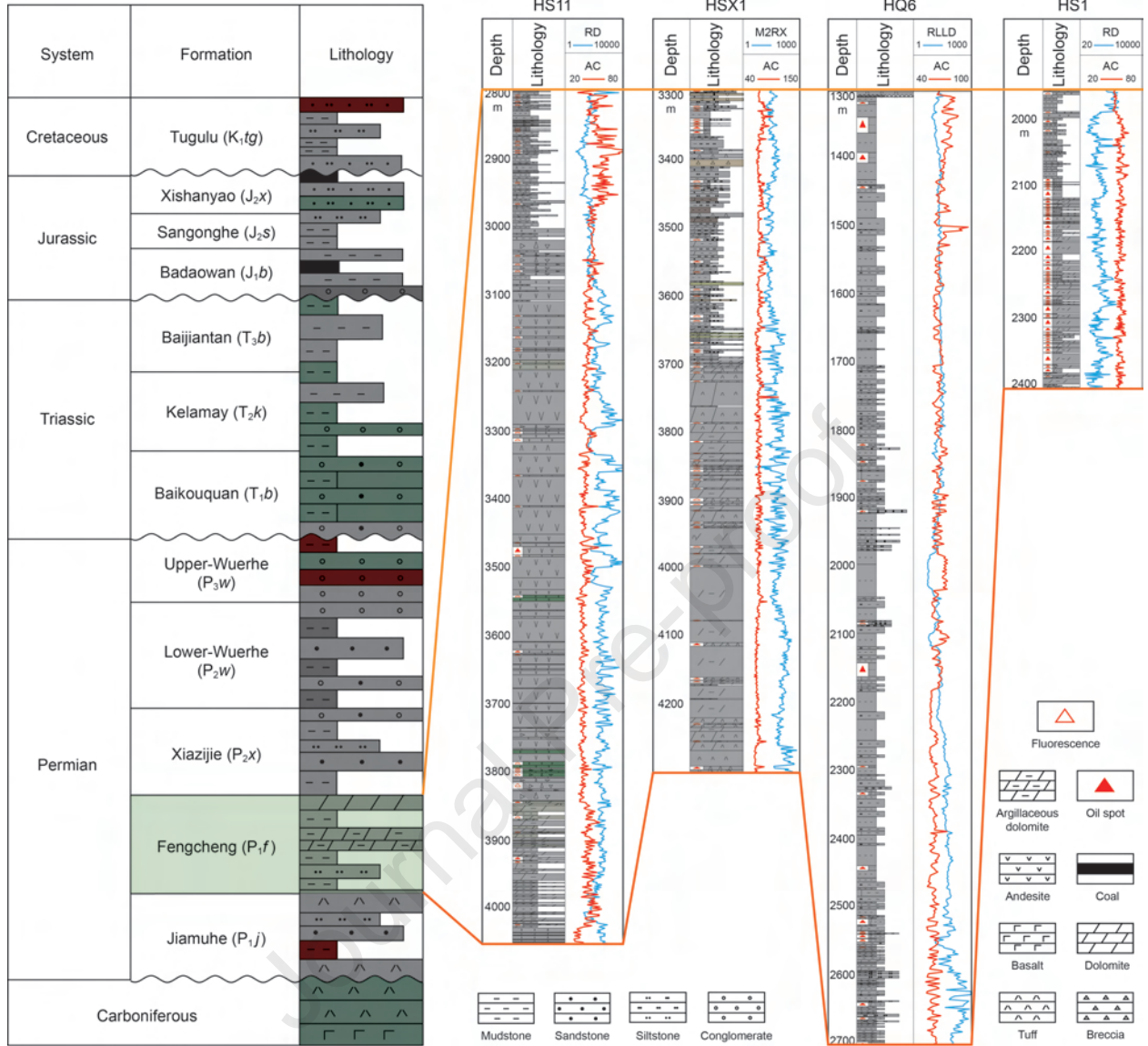
- of organic matter in the Upper Jurassic Madbi shale succession (Masila Basin, Yemen): Origin, type and preservation. *Org. Geochem.* 49, 18–29. <https://doi.org/10.1016/j.orggeochem.2012.05.005>.
- Hu, T., Pang, X.Q., Jiang, F.J., et al., 2021. Key factors controlling shale oil enrichment in saline lacustrine rift basin: implications from two shale oil wells in Dongpu Depression, Bohai Bay Basin. *Petrol. Sci.* (18), 687–711. <https://doi.org/10.1007/s12182-021-00564-z>.
- Hu, T., Pang, X.Q., Y, S., Yang, et al., 2017. Hydrocarbon generation and expulsion characteristics of P₁f source rocks and tight oil accumulation potential of Fengcheng area on northwest margin of Junggar Basin, Northwest China. *J. Cent. S. Univ.* 48(2), 427–439. <https://doi.org/10.11817/j.issn.1672-7207.2017.02.022> (in Chinese).
- Jarvie, D. M., 2012. Shale resource systems for oil and gas: Part 2—Shale-oil resource systems. *AAPG Memoir.* 97, 89–119. <https://doi.org/10.1306/13321447M973489>.
- Jiang, Q.G., Li, M.W., Qian, M.H., et al., 2016. Quantitative characterization of shale oil in different occurrence states and its application. *Petrol. Geol. Exp.* 38(6), 842–849. <https://doi.org/10.11781/sydydz201606842> (in Chinese).
- Jin, Z.J., Zhu, R.K., Liang, X.P., et al., 2021. Several issues worthy of attention in current lacustrine shale oil exploration and development. *Petrol. Explor. Dev.* 48(6), 1276–1287. <https://doi.org/10.11698/PED.2021.06.20> (in Chinese).
- Ju, W., Niu, X.B., Feng, S.B., et al., 2020. Predicting the present-day in situ stress distribution within the Yanchang Formation Chang 7 shale oil reservoir of Ordos Basin, central China. *Petrol. Sci.* 17, 912–924. <https://doi.org/10.1007/s12182-020-00448-8>.
- Lerch, B., Karlsen, D.A., Matapour, Z., et al., 2016. Organic geochemistry of Barents Sea petroleum: Thermal maturity and alteration and mixing processes in oils and condensates. *J. Petrol. Geol.* 39(2), 125–148. <https://doi.org/10.1111/jpg.12637>.
- Li, C.Z., Guo, P., Ke, X.Q., et al., 2021a. Genesis of high-quality source rocks in volcano-related alkaline lakes and implications for the exploration and development of shale oil and gas. *Oil Gas Geol.* 42(6), 1423–1434. <https://doi.org/10.11743/ogg20210616> (in Chinese).
- Li, J.B., Jiang, C.Q., Wang, M., et al., 2020. Adsorbed and free hydrocarbons in unconventional shale reservoir: A new insight from NMR T₁-T₂ maps. *Mar. Petrol. Geol.* 116, 104311. <https://doi.org/10.1016/j.marpetgeo.2020.104311>.
- Li, J.B., Wang, M., Fei, J.S., et al., 2022b. Determination of in situ hydrocarbon contents in shale oil plays. Part 2: Two-dimensional nuclear magnetic resonance (2D NMR) as a potential approach to characterize preserved cores. *Mar. Petrol. Geol.* 145, 105890. <https://doi.org/10.1016/j.marpetgeo.2022.105890>.
- Li, J.B., Wang, M., Jiang, C.Q., et al., 2022a. Sorption model of lacustrine shale oil: Insights from the contribution of organic matter and clay minerals. *Energy* 260, 125011. <https://doi.org/10.1016/j.energy.2022.125011>.
- Li, J.Q., Lu, S.F., Cai, J.C., et al., 2018a. Adsorbed and free oil in lacustrine nanoporous shale: a

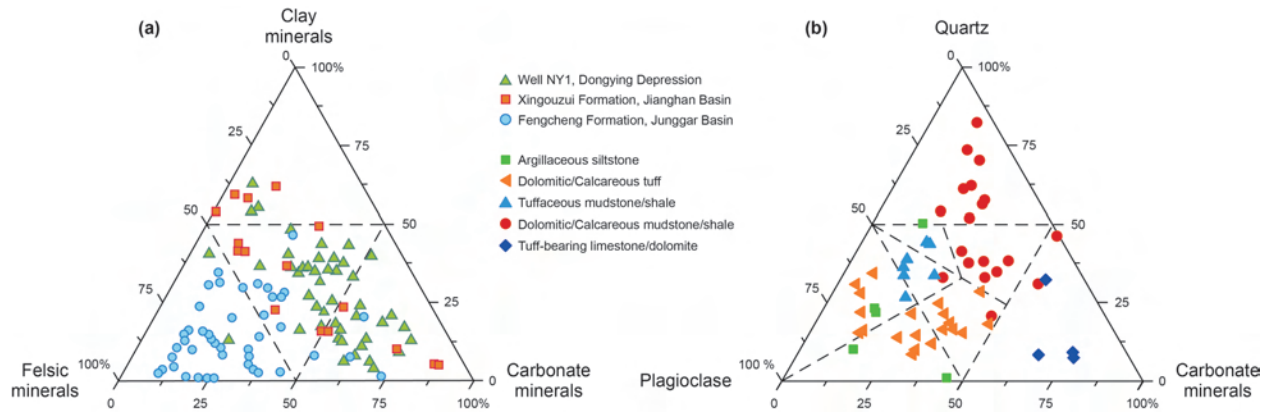
- theoretical model and a case study. *Energy Fuels* 32, 12247–12258. <https://doi.org/10.1021/acs.energyfuels.8b02953>.
- Li, Q.W., Pang, X.Q., Tang, L., et al., 2018b. Occurrence features and gas content analysis of marine and continental shales: A comparative study of Longmaxi Formation and Yanchang Formation. *J. Nat. Gas. Sci. Eng.* 56, 504–522. <https://doi.org/10.1016/j.jngse.2018.06.019>.
- Li, W.H., Kuang, Y.F., Lu, S.F., et al., 2019. Porosity Enhancement Potential through Dolomite Mineral Dissolution in the Shale Reservoir: A Case Study of an Argillaceous Dolomite Reservoir in the Jiangnan Basin. *Energy Fuels* 33, 4857–4864. <https://doi.org/10.1021/acs.energyfuels.9b00486>.
- Li, W.W., Cao, J., Zhi, D.M., et al., 2021b. Controls on shale oil accumulation in alkaline lacustrine settings: Late Paleozoic Fengcheng Formation, northwestern Junggar Basin. *Mar. Petrol. Geol.* 129, 105107. <https://doi.org/10.1016/j.marpetgeo.2021.105107>.
- Li, X.L., Zhang, K.H., Lin, H.X., et al., 2018c. Sedimentary environment and facies of Permian Fengcheng formation in Hashan and its adjacent areas. *Journal of Northwest University (Natural Science Edition)* 48(5), 699–708. <https://doi.org/10.16152/j.cnki.xdxbzr> (in Chinese).
- Liu, B., Sun, J.H., Zhang, Y.Q., et al., 2021. Reservoir space and enrichment model of shale oil in the first member of Cretaceous Qingshankou Formation in the Changling Sag, southern Songliao Basin, NE China. *Petrol. Explor. Dev.* 48(3), 521–535. <https://doi.org/10.11698/PED.2021.03.08> (in Chinese).
- Liu, K.Q., Ostadhassan, M., Zhou, J., et al., 2017. Nanoscale pore structure characterization of the Bakken shale in the USA. *Fuel* 209(1), 567–578. <https://doi.org/10.1016/j.fuel.2017.08.034>.
- Loucks, R.G., Reed, R.M., Ruppel, S.C., et al., 2012. Spectrum of pore types and networks in mudrocks and a descriptive classification for matrix-related mudrock pores. *AAPG Bull.* 96(6), 1071–1098. <https://doi.org/10.1306/08171111061>.
- Loucks, R.G., Reed, R.M., Ruppel, S.C., et al., 2009. Morphology, genesis, and distribution of nanometer-scale pores in siliceous mudstones of the Mississippian Barnett Shale. *Journal of Sedimentary Research* 79, 848–861. <https://doi.org/10.2110/jsr.2009.092>.
- Lu, S.F., Xue, H.T., Wang, M., et al., 2016. Several key issues and research trends in evaluation of shale oil. *Acta Pet. Sin.* 37(10), 1309–1322. <https://doi.org/10.7623/syxb201610012> (in Chinese).
- Lu, S.F., Huang, W.B., Chen, F.W., et al., 2012. Classification and evaluation criteria of shale oil and gas resources: Discussion and application. *Petrol. Explor. Dev.* 39(2), 249–256. [https://doi.org/10.1016/s1876-3804\(12\)60042-1](https://doi.org/10.1016/s1876-3804(12)60042-1) (in Chinese).
- Luo, Q.Y., Gong, L., Qu, Y.S., et al., 2018. The tight oil potential of the Lucaogou Formation from the southern Junggar Basin, China. *Fuel* 234, 858–871. <https://doi.org/10.1016/j.fuel.2018.07.002>.
- Peters, K.E., Cassa, M.R., 1994. Applied source rock geochemistry. *AAPG Memoir.* 60, 93–120.
- Peters, K.E., Walters C.C., Moldowan, J.M., 2005. The biomarker guide, biomarkers and isotopes

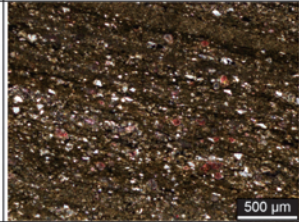
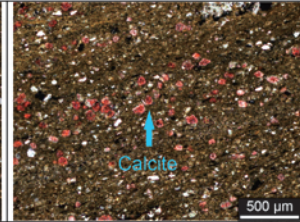
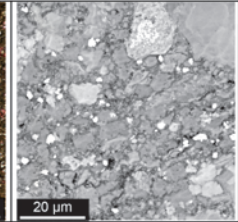
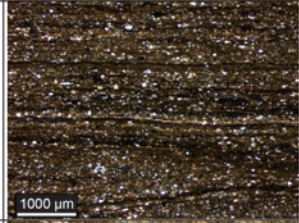
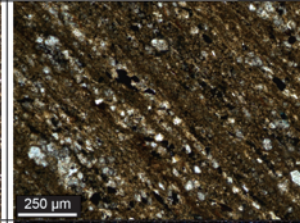
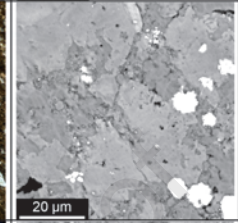
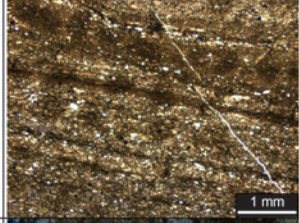

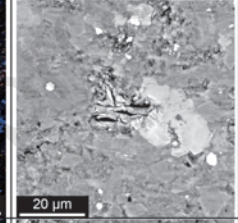
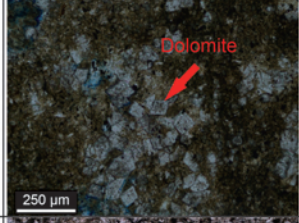
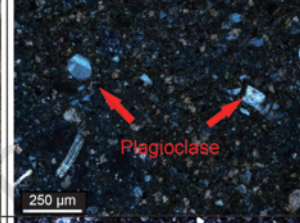
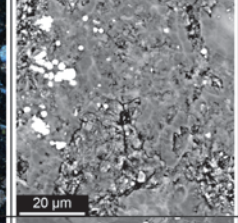
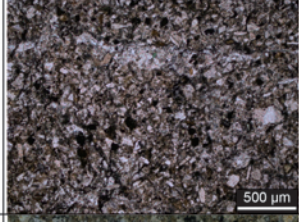
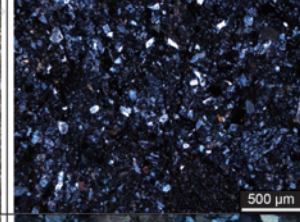
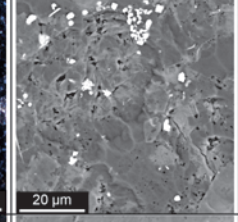
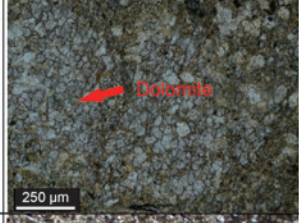
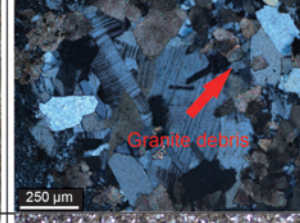
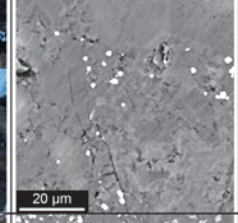
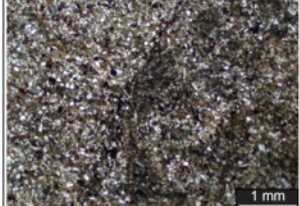

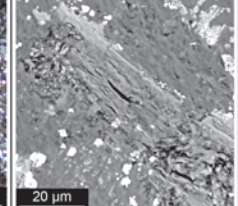
- in petroleum exploration and earth history. 2nd edition. New York: Cambridge University Press, pp. 1–50.
- Ross, D.J.K., Bustin, R.M., 2009. The importance of shale composition and pore structure upon gas storage potential of shale gas reservoirs. *Mar. Petrol. Geol.* 26, 916–927. <https://doi.org/10.1016/j.marpetgeo.2008.06.004>.
- Sonnenberg, S.A., Pramudito, A., 2009. Petroleum geology of the giant Elm Coulee field, Williston Basin. *AAPG Bull.* 93(9), 1127–1153. <https://doi.org/10.1306/05280909006>.
- Tang, Y., Cao, J., He, W.J., et al., 2021. Discovery of shale oil in alkaline lacustrine basins: The Late Paleozoic Fengcheng Formation, Mahu Sag, Junggar Basin, China. *Petrol. Sci.* 18(5), 1281–1293. <https://doi.org/10.1016/j.petsci.2021.04.001>.
- Tissot, B.P., Welte, D.H., 1984. *Petroleum formation and occurrence*. Springer-Verlag. Earth-Sci. Rev.
- Wang, B.Y., Liu, B., Sun, G.X., et al., 2021a. Evaluation of the Shale Oil Reservoir and the Oil Enrichment Model for the First Member of the Lucaogou Formation, Western Jimusaer Depression, Junggar Basin, NW China. *ACS Omega* 6, 12081–12098. <https://doi.org/10.1021/acsomega.1c00756>.
- Wang, S., Wang, G.W., Huang, L.L., et al., 2021b. Logging evaluation of lamina structure and reservoir quality in shale oil reservoir of Fengcheng Formation in Mahu Sag, China. *Mar. Petrol. Geol.* 133, 105299. <https://doi.org/10.1016/j.marpetgeo.2021.105299>.
- Wang, S.Z., Wu, Q.Q., Song, M.Y., et al., 2018. Quantitative evaluation of the transportation of fault zone and its controlling effect on hydrocarbon migration and accumulation: Case study of Hala'alat Mountain tectonic belt in the north margin of Junggar Basin. *Nat. Gas Geosci.* 29(11), 1559–1567. <https://doi.org/10.11764/j.issn.1672-1926.2018.09.002> (in Chinese).
- Yang, F., Ning, Z.F., Wang, Q., et al., 2016a. Pore structure of Cambrian shales from the Sichuan Basin in China and implications to gas storage. *Mar. Petrol. Geol.* 70, 14–26. <https://doi.org/10.1016/j.marpetgeo.2015.11.001>.
- Yang, H., Niu, X.B., Xu, L.M., et al., 2016b. Exploration potential of shale oil in Chang7 Member, Upper Triassic Yanchang Formation, Ordos Basin, NW China. *Petrol. Explor. Dev.* 43(4), 560–569. [https://doi.org/10.1016/S1876-3804\(16\)30066-0](https://doi.org/10.1016/S1876-3804(16)30066-0) (in Chinese).
- Yu, K.H., Cao, Y.C., Qiu, L.W., et al., 2018. The hydrocarbon generation potential and migration in an alkaline evaporite basin: The Early Permian Fengcheng Formation in the Junggar Basin, northwestern China. *Mar. Petrol. Geol.* 98, 12–32. <https://doi.org/10.1016/j.marpetgeo.2018.08.010>.
- Yu, K.H., Cao, Y.C., Qiu, L.W., et al., 2019. Depositional environments in an arid, closed basin and their implications for oil and gas exploration: The lower Permian Fengcheng Formation in the Junggar Basin, China. *AAPG Bull.* 103(9), 2073–2115. <https://doi.org/10.1306/01301917414>.
- Zhang, G.Y., Wang, Z.Z., Guo, X.G., et al., 2019. Characteristics of lacustrine dolomitic rock reservoir and accumulation of tight oil in the Permian Fengcheng Formation, the western slope

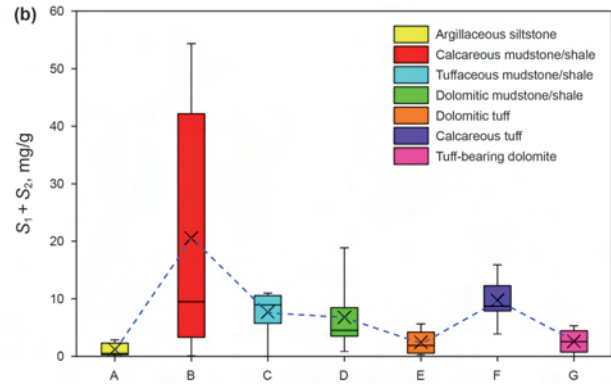
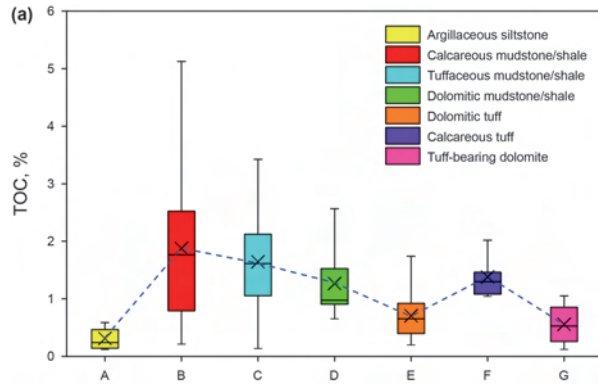
- of the Mahu Sag, Junggar Basin, NW China. *J. Asian Earth Sci.* 178, 64–80. <https://doi.org/10.1016/j.jseaes.2019.01.002>.
- Zhang, J.Y., Sun, M.L., Liu, G.D., et al., 2021a. Geochemical characteristics, hydrocarbon potential, and depositional environment evolution of fine-grained mixed source rocks in the Permian Lucaogou Formation, Jimusaer Sag, Junggar Basin. *Energy Fuels* 35, 264–282. <https://doi.org/10.1021/acs.energyfuels.0c02500>.
- Zhang, L.C., Lu, S.F., Jiang, S., et al., 2018a. Effect of shale lithofacies on pore structure of the Wufeng–Longmaxi shale in southeast Chongqing, China. *Energy Fuels* 32, 6603–6618. <https://doi.org/10.1021/acs.energyfuels.8b00799>.
- Zhang, P.F., Lu, S.F., Li, J.Q., et al., 2020. Broad ion beam-scanning electron microscopy pore microstructure and multifractal characterization of shale oil reservoir: A case sample from Dongying Sag, Bohai Bay Basin, China. *Energy Explor. Exploit.* 38(3), 613–628. <https://doi.org/10.1177/0144598719893126>.
- Zhang, P.F., Lu, S.F., Li, J.Q., et al., 2018b. Petrophysical characterization of oil-bearing shales by low-field nuclear magnetic resonance (NMR). *Mar. Petrol. Geol.* 89, 775–785. <https://doi.org/10.1016/j.marpetgeo.2017.11.015>.
- Zhang, P.F., Lu, S.F., Lin, Z.Z., et al., 2022. Key Oil Content Parameter Correction of Shale Oil Resources: A Case Study of the Paleogene Funing Formation, Subei Basin, China. *Energy Fuels*. <https://doi.org/10.1021/acs.energyfuels.2c00610>.
- Zhang, Y.F., Yuan, X.D., Wang, M., et al., 2021b. Discovery of lacustrine shale deposits in the Yanshan Orogenic Belt, China: Implications for hydrocarbon exploration. *Geoscience Frontiers*. 12(6), 101256. <https://doi.org/10.1016/j.gsf.2021.101256>.
- Zhao, W.Z., Zhu, R.K., Hu, S.Y., et al., 2020. Accumulation contribution differences between lacustrine organic-rich shales and mudstones and their significance in shale oil evaluation. *Petrol. Explor. Dev.* 47(6), 1160–1171. [https://doi.org/10.1016/S1876-3804\(20\)60126-X](https://doi.org/10.1016/S1876-3804(20)60126-X).
- Zhi, D.M., Tang, Y., Zheng, M.L., et al., 2019. Geological characteristics and accumulation controlling factors of shale reservoirs in Fengcheng Formation, Mahu sag, Junggar Basin. *China Petroleum Exploration* 24(5), 615–623. <https://doi.org/10.3969/j.issn.1672-7703.2019.05.008> (in Chinese).

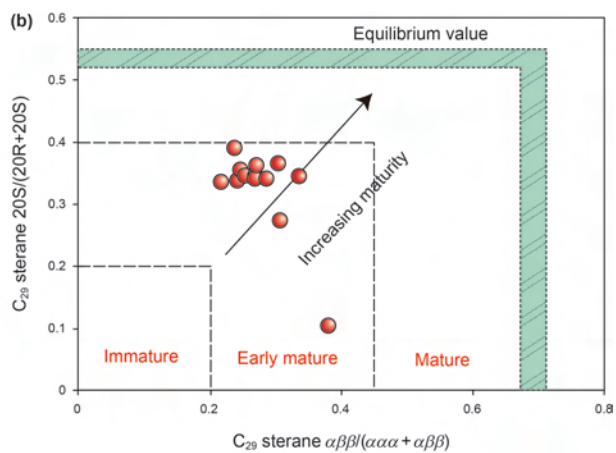
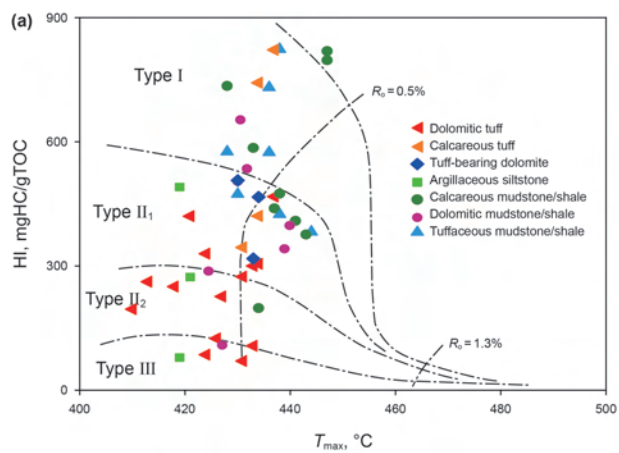


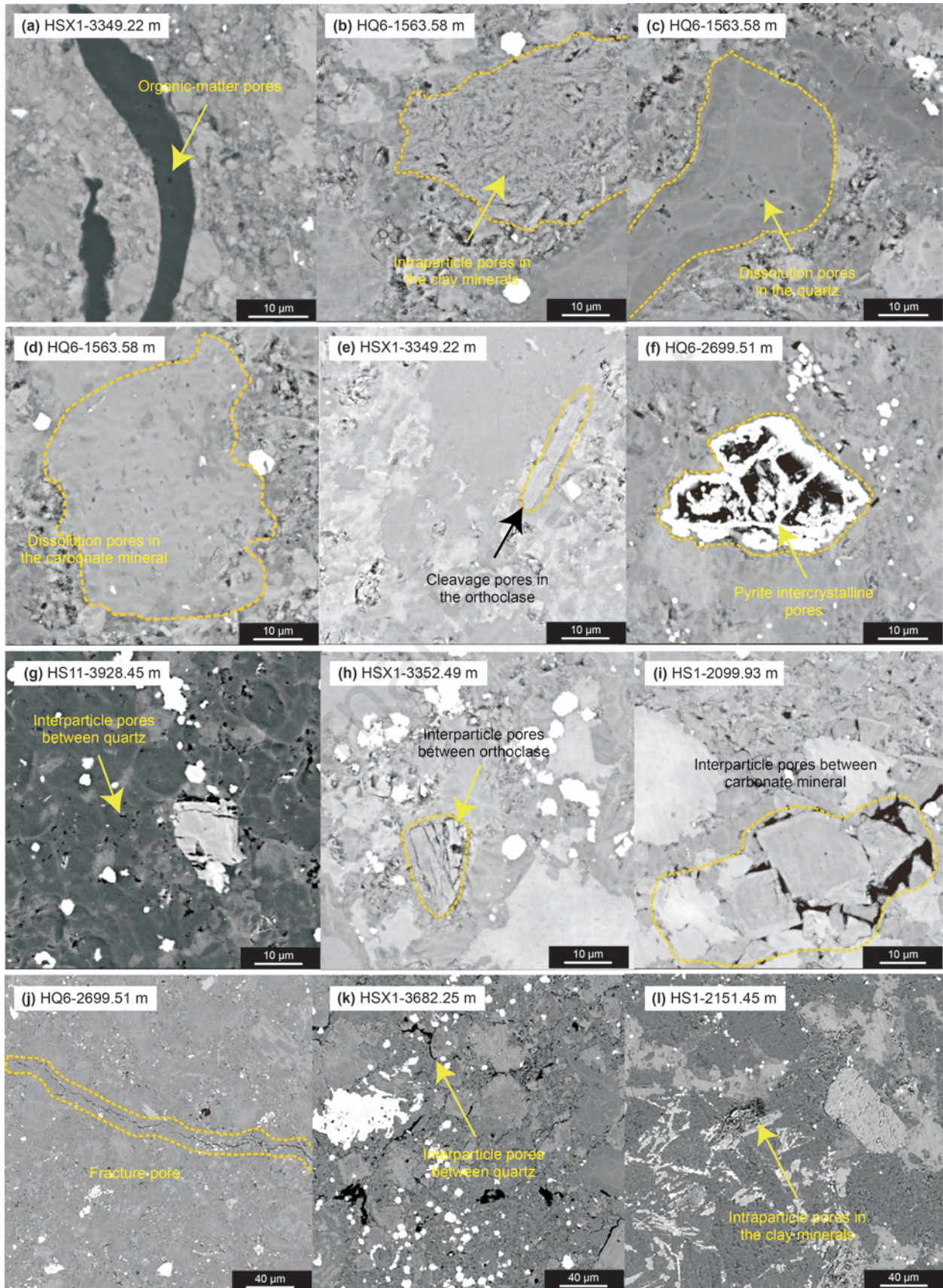




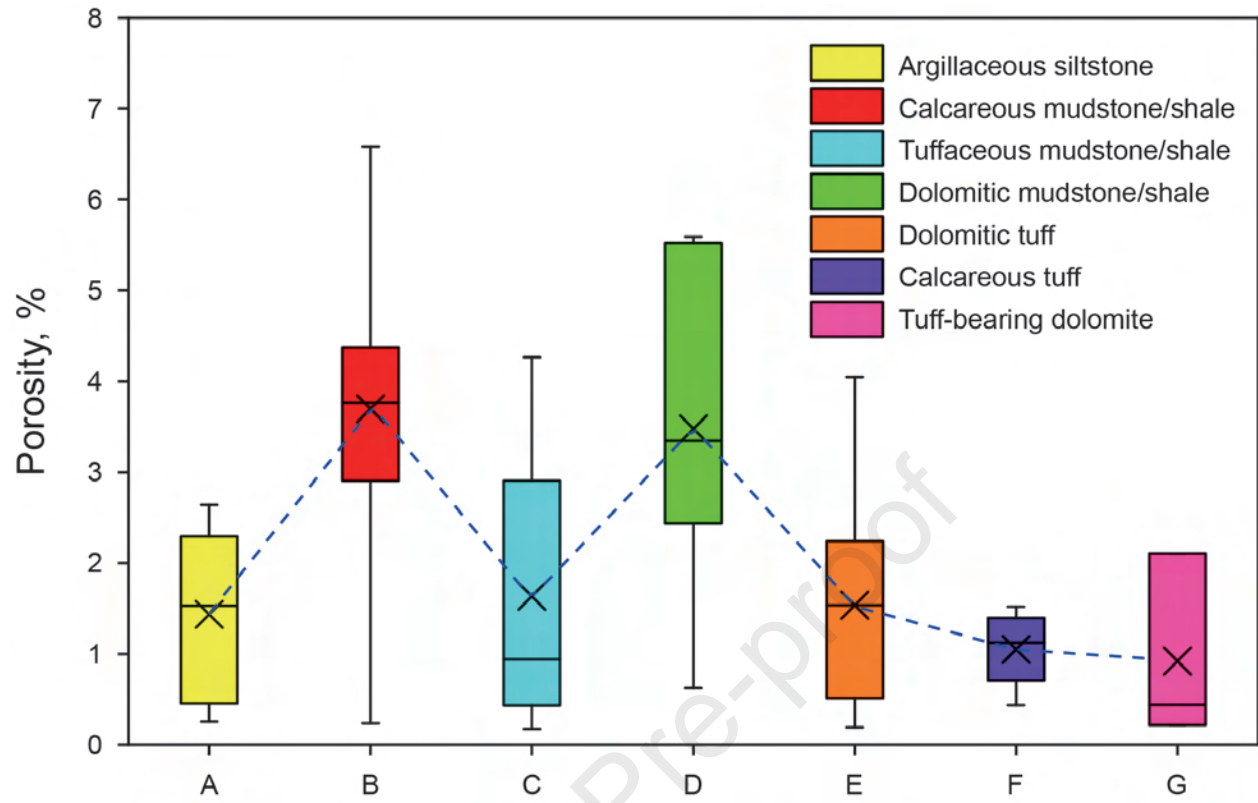
Lithofacies	Characteristics			Description and distribution
Calcareous shale HSX1-7 3349.22 m	 <p>500 μm</p>	 <p>500 μm</p>	 <p>20 μm</p>	Mainly consists of quartz and calcite, calcites are distributed in strips
Dolomitic shale HSX1-14 3682.25 m	 <p>1000 μm</p>	 <p>250 μm</p>	 <p>20 μm</p>	Mainly consists of dolomite and clay minerals, no fractures were found
Tuffaceous shale HS1-8 2101.38 m	 <p>1 mm</p>	 <p>500 μm</p>	 <p>20 μm</p>	Mainly consists of clay minerals, quartz and plagioclase, some calcites were filled between particals
Dolomitic tuff HQ6-13 2541.78 m	 <p>250 μm</p>	 <p>250 μm</p>	 <p>20 μm</p>	Plagioclase >50%, dolomite aggregates were developed, fractures are filled with quartz the content of dolomite is 20–40%
Dolomite-bearing tuff HS11-8 3928.45 m	 <p>500 μm</p>	 <p>500 μm</p>	 <p>20 μm</p>	Plagioclase >50%, the content of dolomite is <20%, no fractures were found
Tuff-bearing dolomite HQ6-20 2699.51 m	 <p>250 μm</p>	 <p>250 μm</p>	 <p>20 μm</p>	Dolomite >40%, calcite and plagioclase are the other two main minerals, many fractures developed, the content of tuff is <20%
Argillaceous siltstone HS1-11 2151.45 m	 <p>1 mm</p>	 <p>1 mm</p>	 <p>20 μm</p>	Grain size of the majority of minerals >10 μm, mainly consists of plagioclase, clay minerals and calcite, no fractures were found

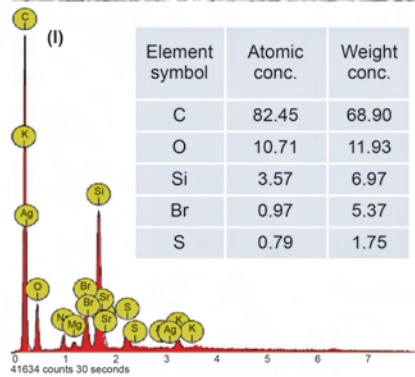
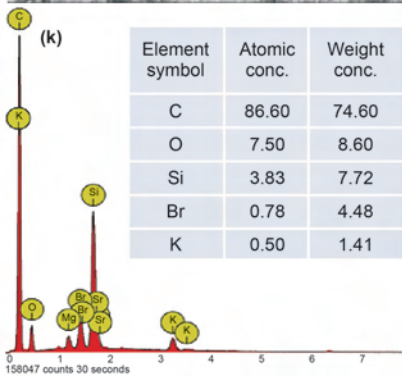
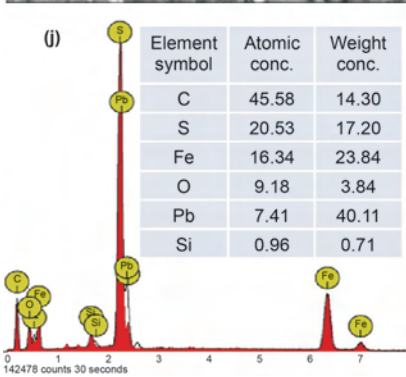
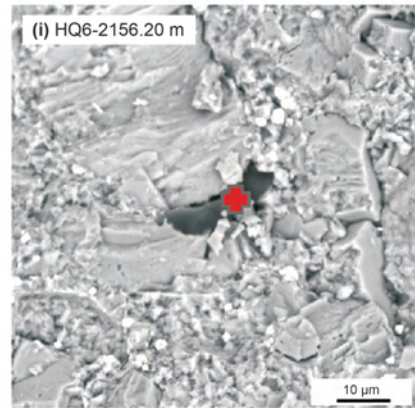
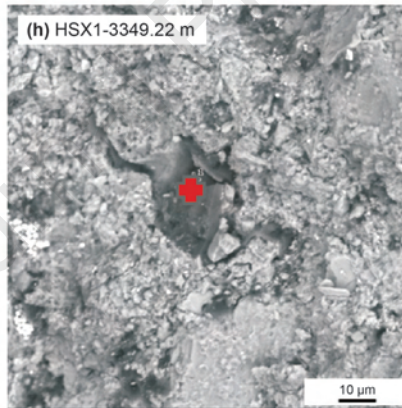
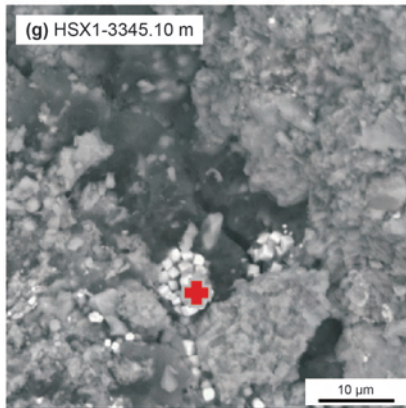
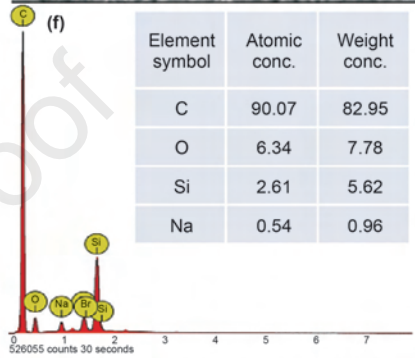
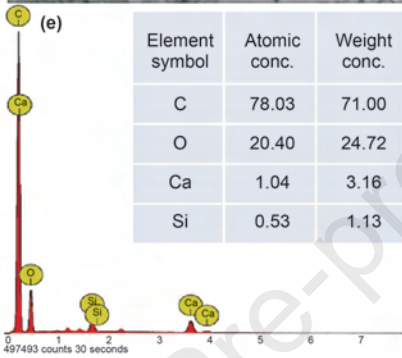
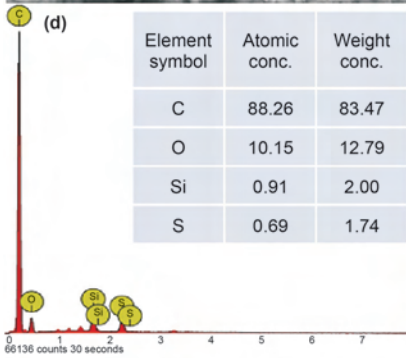
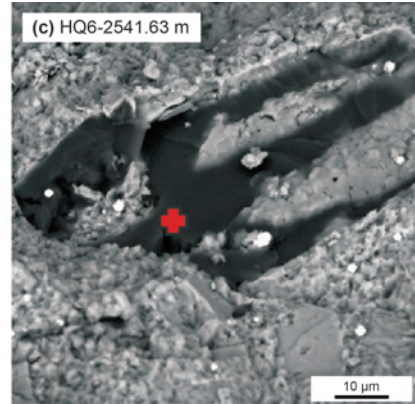
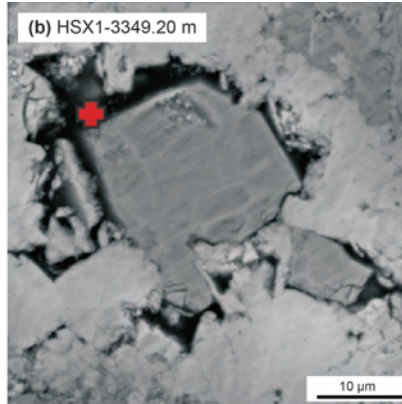
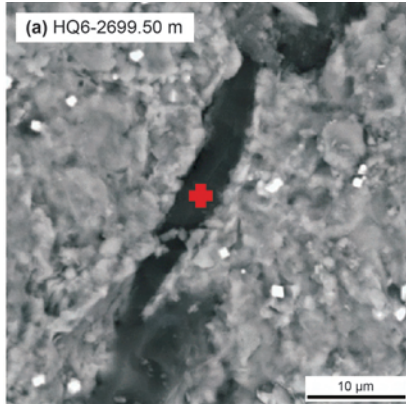


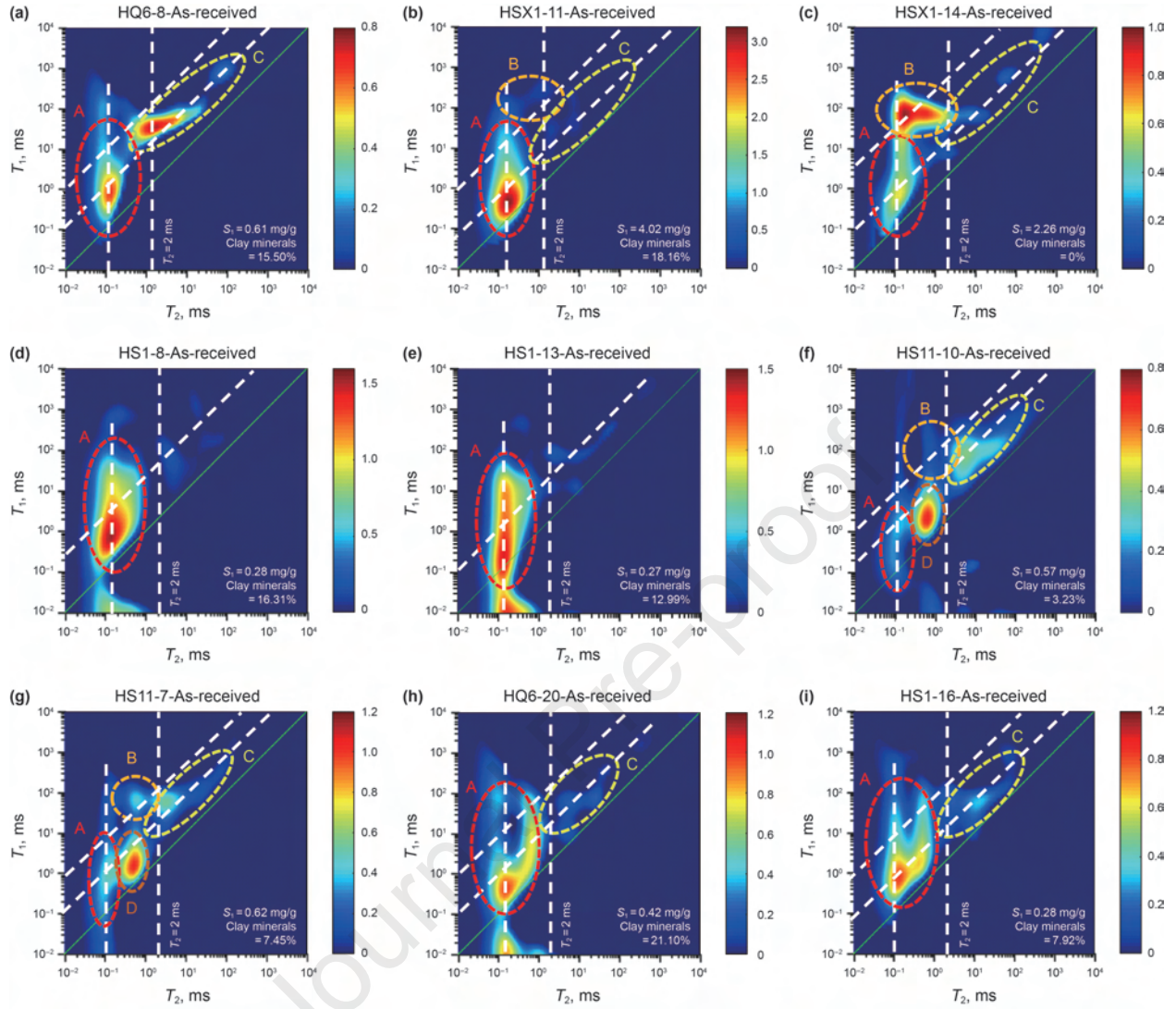


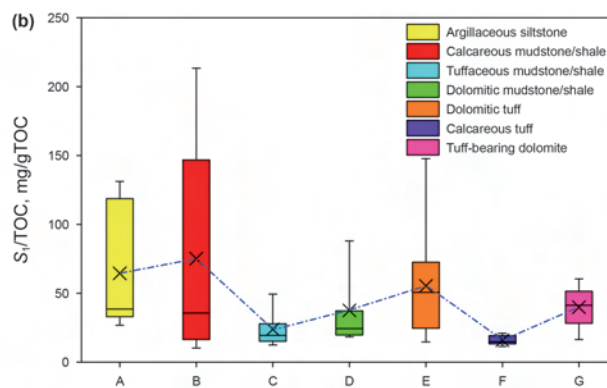
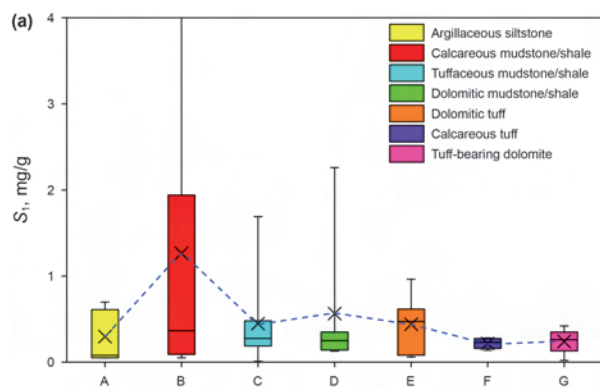


Journal Pre-proof









Journal Pre-proof

